

Deep learning enables urban change profiling through alignment of historical maps

Sidi Wu^a, Yizi Chen^a, Maurizio Gribaudi^b, Konrad Schindler^c, Clément Mallet^d,
Julien Perret^d, Lorenz Hurni^a

^a*Institute of Cartography and Geoinformation, ETH Zurich, Zurich, Switzerland*

^b*CRH, École des hautes études en sciences sociales (EHESS), Paris, France*

^c*Photogrammetry and Remote Sensing, ETH Zurich, Zurich, Switzerland*

^d*LASTIG, Univ Gustave Eiffel, IGN, Géodata Paris, Paris, France*

Abstract

Prior to modern Earth observation technologies, historical maps provide a unique record of long-term urban transformation and offer a lens on the evolving identity of cities. However, extracting consistent and fine-grained change information from historical map series remains challenging due to spatial misalignment, cartographic variation, and degrading document quality, limiting most analyses to small-scale or qualitative approaches. We propose a fully automated, deep learning-based framework for fine-grained urban change analysis from large collections of historical maps, built on a modular design that integrates dense map alignment, multi-temporal object detection, and change profiling. This framework shifts the analysis of historical maps from ad hoc visual comparison toward systematic, quantitative characterization of urban change. Experiments demonstrate the robust performance of the proposed alignment and object detection methods. Applied to Paris between 1868 and 1937, the framework reveals the spatial and temporal heterogeneity in urban transformation, highlighting its relevance for research in the social sciences and humanities. The modular design of our framework further supports adaptation to diverse cartographic contexts and downstream applications.

1. Main

The last two centuries have witnessed unprecedented modernization and urbanization. Analyzing urban change is pivotal to understanding these long-term dynamics, as cities continuously evolve in response to infrastructural expansion, shifting demographics, and policy decisions. By examining how cities transform across space and times, researchers can uncover mechanisms that shape urban development, thereby developing more sustainable and resilient development strategies [1, 2]. Most studies of urban change focus on the past 50 years [3, 4, 5], largely because of the availability of satellite imagery and digital geographic records. Yet many of the most consequential transformations occurred earlier, especially during the 19th and early 20th centuries, when modern planning principles were first introduced. For instance, the transformation of Paris during the second French Empire (so-called *Haussmannian transformations*) in the mid-19th century was a pioneering

and influential project, with effects that extended well into the 20th century. This project reshaped Paris from a congested medieval city into a modern metropolis by introducing wide boulevards, harmonized building façades, improved sanitation, and expanded public spaces such as parks and squares. Another pioneer project, the *Eixample plan* of Barcelona, initiated in the mid-19th century, introduced a grid-based layout with wide, uniform streets, abundant open spaces, and mixed-use building blocks that balanced practical functionality with aesthetic appeal. A further example is the unification of Switzerland as a federal state in 1848, which accelerated nationwide railway construction, spurred urban growth, and supported the development of public infrastructure. Characterizing patterns of change in the early modernization period provides us a crucial historical lens and a more holistic view of the cities' identity as a continuation of past transformations, rather than a series of isolated developments.

Thanks to advances and large-scale applications of geodetic surveying and cartography methods in the last two centuries, topographic and cadastral maps have been produced with high geometric accuracy, rich detail, and regular updates every decade in response to ongoing landscape and urban changes. For example, *Atlas Municipal*, a collection of city planning maps of Paris and its suburbs, meticulously documented buildings, building blocks, and other urban infrastructures such as parks and public spaces in high resolution from the mid-19th century to the early 20th century, providing a valuable record of the early modernization efforts. *Siegfried Maps*, the topographic atlas of Switzerland, produced between the mid-19th and mid-20th centuries, offer a comprehensive and precise representation of Swiss territory, shaped by national unification and infrastructural growth. Analog maps, as the only spatially explicit source available before the advent of modern Earth observation techniques, have been scanned, geo-referenced, and digitally archived in recent years. Notable collections include the USGS Topographic Maps¹ and the David Rumsey Map Collection². These historical maps have been increasingly utilized to reconstruct past landscapes, analyze long-term spatial transformations, and study urban and environmental evolution [8, 9, 10, 11].

Traditionally, detecting changes from historical maps has relied on manual, qualitative, or semi-automatic inspection [8, 11, 10], or has focused only on large-scale summary statistics such as road density and total distance [9, 12]. In recent years, deep-learning-based approaches have been explored to automate feature extraction for buildings, roads, rivers, and forests [13, 14, 15, 16, 17]. However, extracted features often misalign across time, even after being geo-referenced/-located in the same coordinate system, primarily due to surveying errors, cartographic generalization, variations in production methods, storage-induced distortions, and changes in feature signatures over time [18]. This fails to capture fine-grained changes at specific past

¹<http://ngmdb.usgs.gov/maps/TopoView/>

²<http://www.davidrumsey.com/>

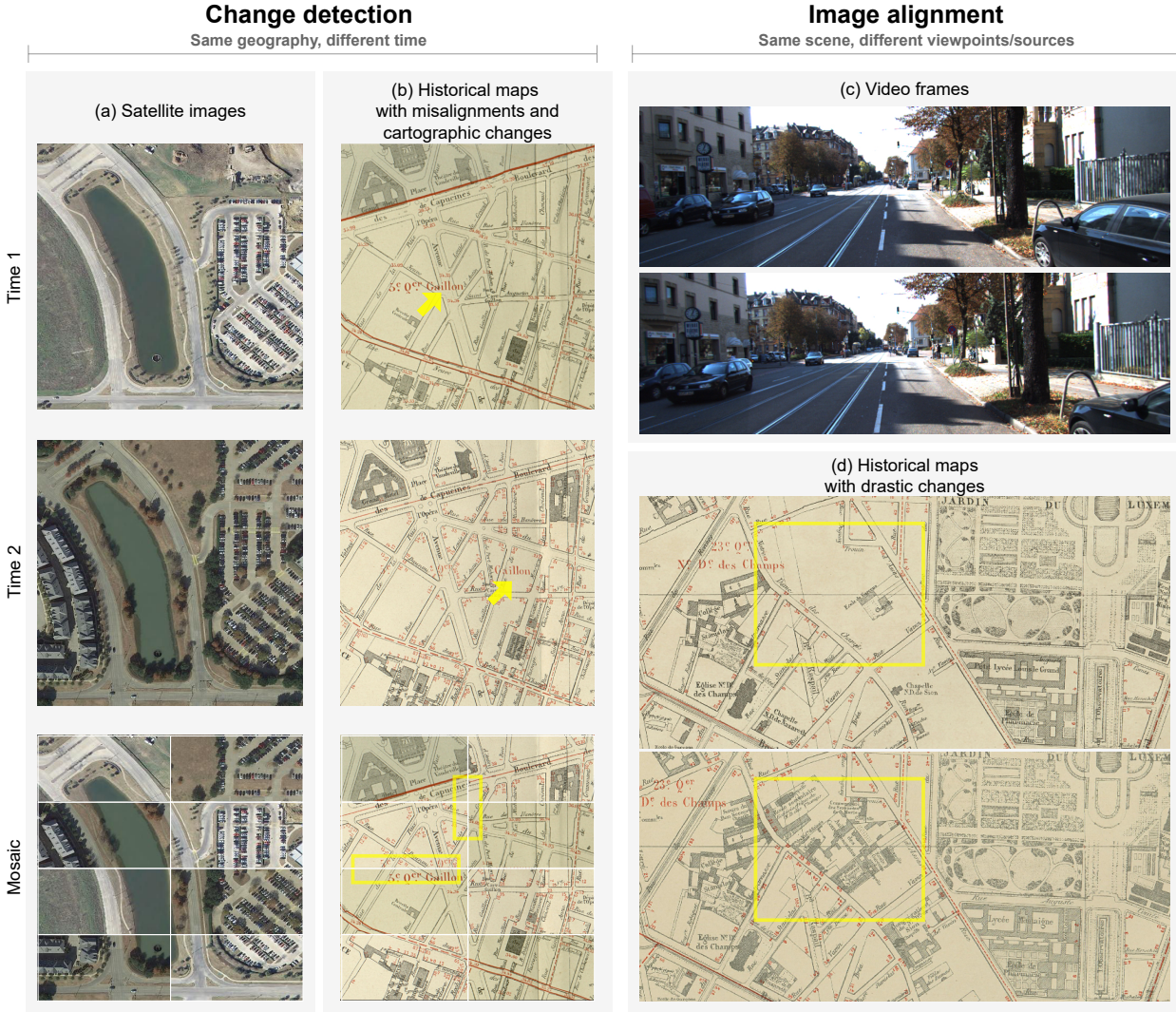


Figure 1: Historical maps violate assumptions underlying standard change-detection and image-alignment methods. (a) Two satellite images [6] with a time difference of 5-10 years exhibit stable object locations across years, allowing simple overlays to reveal changes. (b) Historical maps from editions a decade apart display obvious object misalignment: object locations shift across sheets (yellow boxes at mosaic boundaries), making direct comparison unreliable. In addition, cartographers frequently adjust text labels for layout or legibility (yellow arrows), introducing displacements unrelated to real-world change. (c) Video frames [7] contain smooth, coherent motions where dense-matching algorithms are typically used to align frames, track objects, and estimate per-pixel motion trajectories. (d) Conversely, historical maps exhibit substantial content changes (yellow boxes). These drastic changes, together with deliberate cartographic layout adjustments, undermine the assumptions of dense-matching algorithms, *i.e.*, stable object correspondences for accurate image alignment.

dates and prevents reliable qualitative and quantitative analyses over long time frames. Despite advancements in neural network-based change detection [19, 20, 21, 22, 23, 24], most existing methods are designed for multi-temporal satellite images, where objects are typically assumed to occupy the same position across time—an assumption that does not hold for historical maps, illustrated in Figure 1 (a)(b). Moreover, these approaches usually require predefined concepts of “change”, which can be subjective and strongly dependent on research questions, spatial scale, and temporal context. For historical maps, changes are often subtle and the “truth” of past transformations is uncertain, imposing such rigid definitions can overlook important nuances. This highlights the need for more flexible approaches.

Detecting changes from historical maps therefore require precise spatial alignment of objects, robust object detection methods that can handle graphic variations across decades, and a flexible way of categorizing change. While many studies have developed neural networks to estimate how objects shift between images at the pixel level [25, 26, 27, 28, 29, 30, 31, 32, 33, 34, 35, 36], often referred to as *dense matching*, aligning historical map objects presents unique challenges (Figure 1): the underlying city can change substantially, and cartographers frequently shift text labels and symbols for layout or legibility reasons, complicating correspondence estimation. We therefore argue that a suitably designed, yet not over-engineered, deep learning approach is necessary to leverage information available and retrieve objects in each map, while ensuring consistency and spatial alignment through the full series. We assume that agnostic change profiling can be decomposed into two independent components: spatial alignment and fine-grained object extraction. Further quantitative or qualitative analyses addressing specific historical or urban research questions require dedicated spatial analysis tools and domain expertise and are therefore beyond the scope of this work. To address the mentioned challenges, we embed explicit cartographic guidance into the alignment network during training in a resource-efficient way. To make object detection robust to graphic variations, particularly where older maps suffer from quality degradation, we incorporate multi-temporal information from neighbouring years, allowing the model to resolve ambiguities using additional context. Together, these rigorous alignment and object detection across time enable us to automatically quantify changes by simply comparing overlaps between corresponding objects.

To the best of our knowledge, this is the first fully automated method that can systematically track and measure detailed changes in historical maps over space and time, addressing key technical challenges that have so far been largely overlooked. It substantially reduces the need for exhaustive manual delineation and ad hoc visual comparison, and produces map objects that are directly comparable across years. We demonstrate its effectiveness by tracking urban changes associated with early modernization in Paris between 1868 and 1937, and we show that the proposed alignment model can also be used for related tasks, such as analyzing map distortions and aligning different map series. The resulting aligned objects and change maps

provide a structured basis for detailed studies of urban change, enabling comparative, long-term analyses that can support a broad range of historical, urban, and environmental research.

2. Results

2.1. Overview of the framework

Historical maps provide unique records of long-term urban evolution, but their analysis is fundamentally challenged by severe geometric misalignments and significant diversity (e.g., cartographic variations). To address these challenges, we introduce a unified computational framework that enables dense alignment and fine-grained change detection across historical map editions. An overview of the proposed pipeline is shown in Figure 2. Our framework consists of three main stages: map alignment, instance-level extraction, and fine-grained change analysis. The two first steps are designed to be agnostic to any quantitative and qualitative analysis, while the last one is presented here to illustrate the high relevance of such generic outputs for social and human sciences. As shown in Figure 2 (a), given geo-referenced historical map archives, we first rectify maps depicting the same locations into a common image plane by unifying spatial resolution, cropping to the same extent, and converting geographical coordinates into pixel coordinates with a shared origin. This enables subsequent dense alignment across map editions and suitable qualitative and quantitative assessment for thematic end-users. We then estimate dense displacement fields between map pairs and use them for precise pixel-wise alignment. Based on the aligned maps, an instance detection network identifies urban infrastructures such as buildings, building blocks, and parks. Changes are detected by directly comparing instance geometries across time.

Figure 2 (b) illustrates the **displacement estimation component** of our framework. Since ground-truth displacement fields between historical maps are not available, we adopt a self-supervised deep learning training strategy inspired by [29]. During training, we synthesize paired images with known displacement fields by applying combinations of geometric transformations, which are used to supervise the displacement estimation deep-learning-based network. To adapt the model to real historical maps, we further refine displacement predictions by enforcing *triplet cycle consistency* across multiple images, including both the real image pair and synthetically warped image. The real image pair consists of small patches cropped from maps of different years at the same geographic location. To explicitly account for the challenges posed by historical maps, we simulate drastic object changes and cartographic modifications of text labels during training. Section 2.2 shows the effectiveness of the proposed displacement estimation and map alignment method.

For **instance extraction**, we extract **building units** as individual instances for small map patches (Figure 2 (c)). To improve robustness against graphic defects and local ambiguities, we incorporate temporal

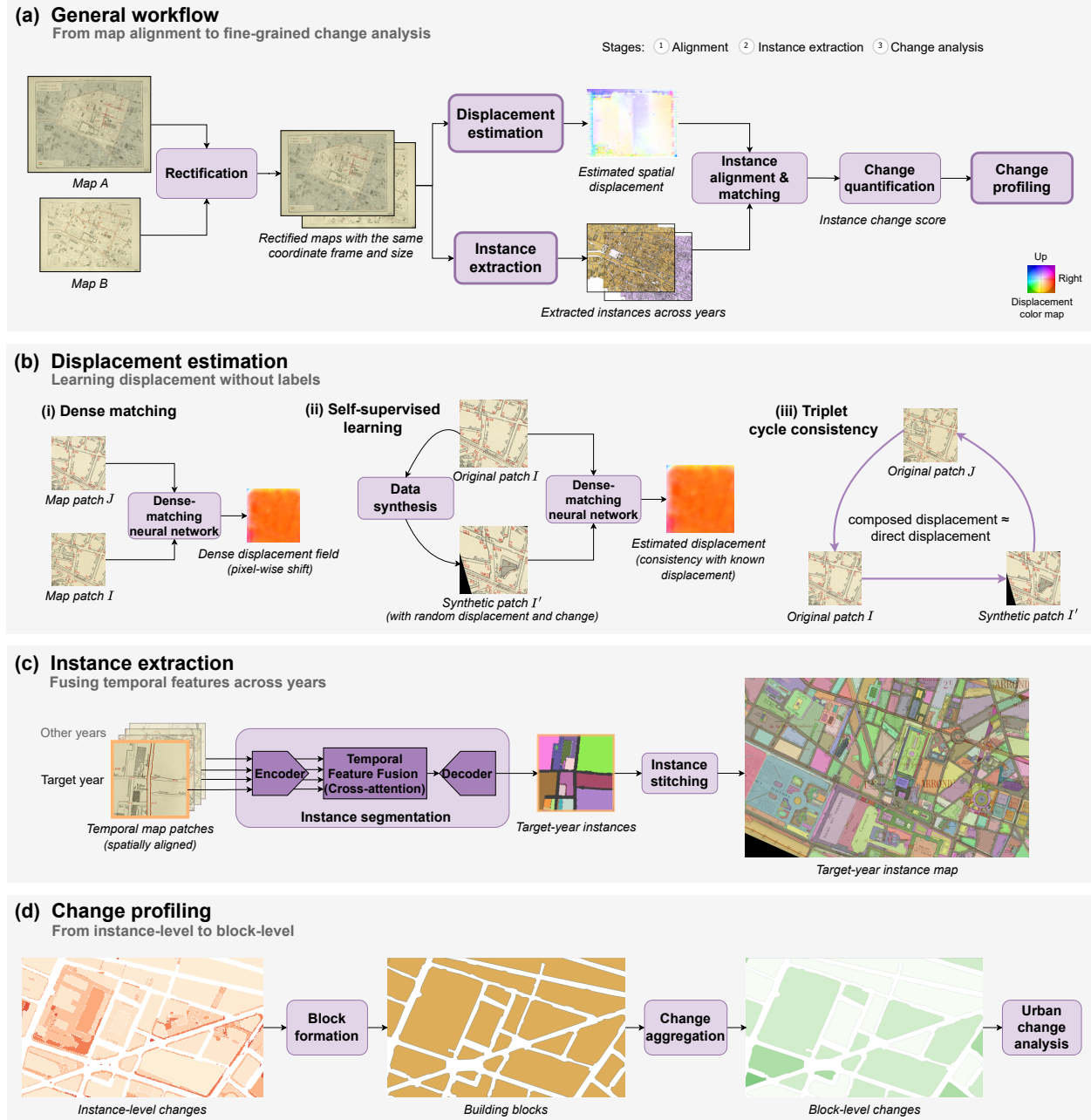


Figure 2: **Method overview.** (a) Workflow for historical map alignment and change analysis. Maps covering the same location are first rectified to a common image plane. For map pairs from different editions (years), we estimate a dense displacement field for pixel-level alignment and extract urban instances for each edition. The displacement field is used to align and match instances across years, enabling fine-grained instance-level change analysis. (b) Dense displacement estimation without ground-truth correspondences. A dense-matching network is trained using self-supervision from synthetic transformations with known displacements, and refined with a triplet cycle-consistency constraint linking real and synthetic views. (c) Instance extraction with temporal knowledge. A shared encoder-decoder integrates information from multiple years via temporal feature fusion to predict instance segmentation for the target year. The patch-wise predictions are stitched to produce a complete instance map. (d) Instance-level changes are aggregated into urban blocks, a fundamental spatial unit in urban morphology and planning, to derive block-level change profiles. These profiles enable planning-relevant interpretation of long-term urban morphological change.

information from multiple map editions. After aligning maps using the estimated displacement field, we fuse features from corresponding locations across time using a temporal integration mechanism inspired by [37]. Patch-wise predictions are subsequently merged to produce **complete instance maps for each year**. Section 2.3 presents the effectiveness of our instance extraction method.

While instance-level comparisons enable detailed change detection, individual instances may represent either entire buildings or partial building elements, which can fragment change analysis. To make the results more interpretable and coherent, **we aggregate detected changes at the level of building blocks, which are more meaningful spatial units aligned with the interpretive practices of urban historians and urban planners** (Figure 2 (d)). To this end, we derive the change profiles of Paris from 1868 to 1937, as demonstrated in Section 2.4.

2.2. Accuracy of dense map alignment

Our self-supervised displacement estimation method extends the WarpC-GLU-Net framework [29] by introducing a self-synthesis strategy that integrates cartographic knowledge, enabling learning from large archival collections without ground-truth displacement annotations. We evaluate alignment performance both within the training area and in previously unseen regions to assess spatial generalizability. We compare our method with two state-of-the-art dense image-matching approaches, GLU-Net [27] and WarpC-GLU-Net (hereafter WarpC), designed to handle large displacements through self-supervised learning strategies. WarpC serves as a strong baseline, as it does not incorporate cartographic simulations, allowing us to isolate the impact of our domain-specific adaptations. More details of the state-of-the-art dense image-matching approaches can be found in Supplementary Note 4.

In the absence of per-pixel ground-truth, we evaluate performance indirectly by assessing alignment at the image and object levels, after applying the estimated displacement fields. At the image level, we measure the similarity between aligned maps using the Structural Similarity Index Measure (SSIM). At the object level, we evaluate alignment accuracy using the Chamfer Distance (CD) between corresponding objects. To reduce the influence of genuine urban changes and outliers, we exclude the top 10%, 20%, and 40% of CD values: the large object distances can be treated as indicators of true change. Beyond alignment accuracy, we assess the smoothness and temporal consistency of the estimated displacement fields, which are critical for stable change analysis. Spatial smoothness is quantified using the mean variation (mV), defined as the average absolute gradient between neighboring pixels. Temporal consistency is evaluated by computing the L1 difference between displacement fields estimated from consecutive year triplets (*e.g.*, 1900–1912–1925).

As summarized in Table 1, all methods substantially reduce object misalignment in both training and unseen test areas, demonstrating strong performance and spatial generalizability. Compared to WarpC, our

Table 1: **Model performance for displacement estimation** in both training areas (15 districts) and unseen testing areas (5 districts). We measure the CD by removing the 10%, 20%, and 40% largest distances. Smoothness is evaluated by mV, and temporal consistency by L1 within triplets from consecutive years. Arrows indicate the direction of better performance.

Method	Image		Object		Disp.	Temp.	Cons.
	SSIM↑	CD(10%)↓	CD(20%)↓	CD(40%)↓	mV↓	L1↓	
TRAINING AREA							
Unaligned	0.72	5.50	3.96	1.89	—	—	
GLU-Net	0.78	2.57	1.73	0.82	0.66	7.16	
WarpC	0.83	1.47	0.95	0.44	0.29	3.87	
Ours	0.83	1.44	0.93	0.43	0.23	2.83	
TESTING AREA							
Unaligned	0.80	3.29	1.54	0.31	—	—	
GLU-Net	0.85	2.12	1.45	0.68	0.54	5.17	
WarpC	0.88	1.20	0.80	0.35	0.23	2.46	
Ours	0.88	1.19	0.79	0.34	0.19	1.73	

method achieves comparable alignment accuracy, while producing markedly smoother displacement fields with substantially higher temporal consistency. **These properties are essential for minimizing jitter and ensuring reliable downstream change quantification.** Qualitative results further support these findings (Figure 3). While all methods successfully align maps with large initial displacements (**a-c**), competing approaches exhibit noticeable distortions when text elements are randomly displaced (**d-e**), or when structural changes occur (**f-g**). In contrast, our method remains stable under both conditions, maintaining coherent alignments even in the presence of extreme cartographic and structural variations (**h**). Qualitative comparison of estimated displacement fields can be found in Supplementary Fig. S4.

2.3. Instance extraction performance

Reliable instance extraction is essential for downstream change analysis. We adopt Mask2Former [38], a state-of-the-art transformer-based instance segmentation framework, as our baseline to identify building units—defined as closed-shape polygons in our approach. Mask2Former already performs well on historical maps. Still, graphic defects and missing details can degrade performance. To improve robustness, we integrate multi-temporal information from multiple map editions, leveraging complementary cues across time, mitigating local ambiguities, and improving the temporal consistencies across editions.

We evaluate instance extraction performance using average precision (AP), computed by aggregating predictions across all available years to jointly assess spatial accuracy and temporal stability. Figure 4 compares AP scores obtained using single-map inference with those from our multi-temporal fusion strategy, stratified by object size. While Mask2Former struggles to detect small objects (area $< 500 \text{ m}^2$), it performs reliably on medium, large, and non-small categories, far more relevant for urban change analysis. Accordingly,

Image		Overlay of aligned images			
Year 1	Year 2	Original	Ours	WarpC	GLUNet
(a)					
(b)					
(c)					
(d)					
(e)					
(f)					
(g)					
(h)					

Figure 3: **A qualitative comparison of image alignment across different methods.** In (a-c), all methods effectively align images despite large displacements between the originals. Our method shows robustness to text displacements in (d) and (e), as well as to object changes in (f-h), maintaining stability even in extreme cases, as seen in (e).

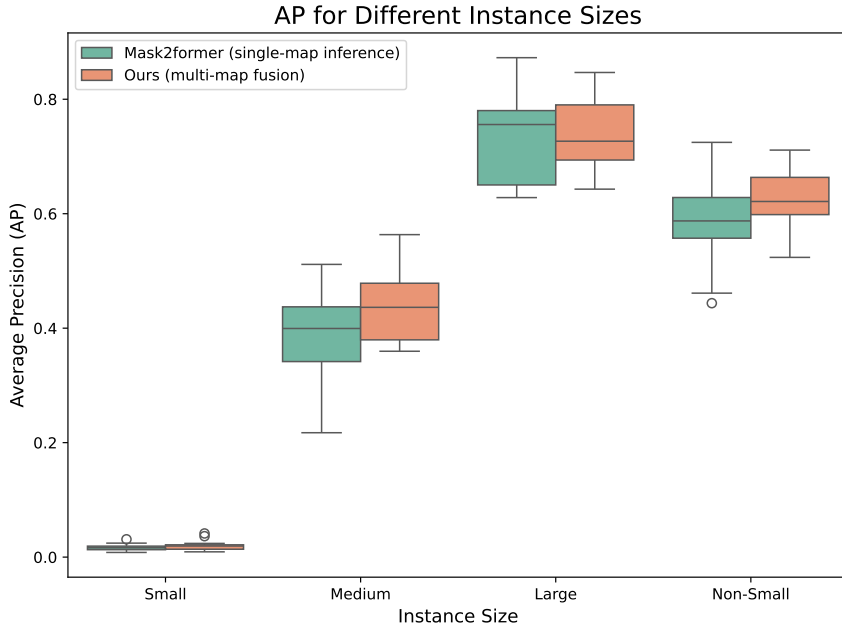


Figure 4: Average precision score for different objects categorized by their areas: small ($\text{area} \leq 500 \text{ m}^2$), medium ($500 \text{ m}^2 < \text{area} < 2000 \text{ m}^2$), large ($\text{area} > 2000 \text{ m}^2$), and non-small ($\text{area} > 500 \text{ m}^2$). We compare using single maps (Mask2former as the baseline) and using our proposed multi-map fusion strategy. Our model improves the overall accuracy and reduces the interquartile range and number of outliers.

we focus on objects larger than 500 m^2 in subsequent experiments. Incorporating multi-temporal information consistently improves AP and reduces variability across years, as reflected by a smaller interquartile range and fewer outliers. These improvements are particularly pronounced for medium-sized buildings, which are more susceptible to graphic degradation and partial occlusion.

Qualitative examples are shown in Figure 5. While the baseline Mask2Former already handles open-border structures such as sidewalks in (a) effectively, our approach demonstrates improved robustness in challenging scenarios where building outlines are faded or partially missing in (d) and (e). This increased stability is **critical for reducing spurious change detections** arising from differences in map quality across years. For subsequent change analysis, individual building units are aggregated into building blocks by uniting connected instances and applying morphological post-processing to remove small holes and filter out blocks below an area threshold of 500 m^2 .

2.4. Fine-grained change profiles of Paris

We aggregated individual building instances into building blocks (or urban blocks) defined by the road network and quantified temporal change using an Intersection over Union (IoU)-based indicator. Such an aggregation is made possible since buildings are exactly delineated: the adequate scale change (blocks) and the detection of the road network are now possible and consistent through the epochs. For each pair of

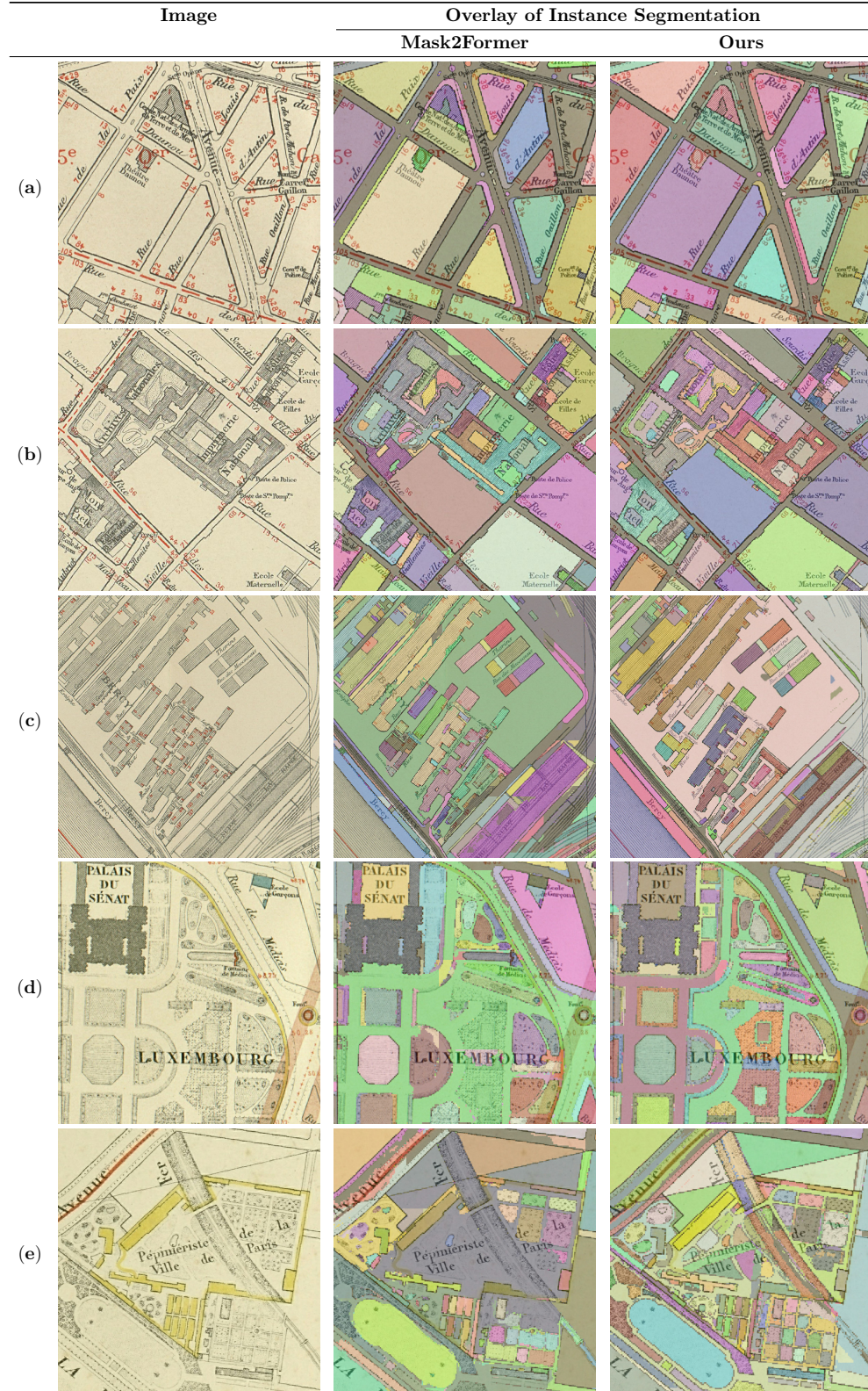


Figure 5: **Qualitative results of our instance extraction method.** Individual instances are shown in distinct colors. Our model performs comparably or slightly better to the baseline Mask2Former in (a) building blocks and sidewalks, (b) intricate building structures, and (c) railway neighborhoods, (d,e) while demonstrating clearly improved performance in detecting faded features such as buildings and gardens.

consecutive years, instances from aligned map sheets were matched using a one-to-one Hungarian assignment, and IoU values were computed for each matched pair. The block-level change indicator was then obtained by averaging IoU scores within each block. Lower values indicate greater structural transformation and thus serve as a proxy for urban change intensity.

Across the full study period, change intensity is highly uneven in both space and time in Figure 6. The decade spanning 1868–1878 stands out as the period of most intensive transformation, with systematically lower IoU values than in subsequent periods. This phase corresponds to a time of major reorganization following the annexation of peripheral areas to Paris in 1860, shown in gray in Figure 6g. These areas, also called *Paris Zone* (zone suburbaine or petite banlieue) [39], correspond to the zone between the Wall of the *Fermiers généraux* (black line) and the Thiers enclosure (the extent of the map). They exhibit stronger and more persistent restructuring throughout the study period than central Paris (the city prior to 1860), shown in orange in Figure 6g. By contrast, central Paris underwent relatively limited modifications and remained mostly stable after 1912 (when the Thiers fortifications were demilitarized). Instead of a global transformation, most of these changes are concentrated on certain areas.

As illustrated in Figure 6h, the modifications of outskirts are associated with infrastructure-oriented zones, particularly zones related to rail freight (in pink) and to waterborne freight and livestock activities (in blue). These areas experienced sustained change over multiple decades, reflecting continuous developments such as the construction of new tracks, facilities, and associated buildings. In the meanwhile, other peripheral areas were spared from the extensive restructurings, as shown in yellow. These relatively stable zones include former villages, such as *Passy* and *Les Batignolles*, that were gradually and organically integrated into the urban fabric, as well as newly planned districts such as *Beau-Grenelle* and parts of *Belleville*.

The modifications of central Paris, as shown in Figure 6i, are also confined to specific sites that can be grouped into several categories: hospitals (in yellow), parks (in green), railway stations (in pink), and a small number of other public buildings (e.g., prisons and military facilities, in blue). Additionally, areas shown in orange correspond to developments associated with the Paris World's Fairs (*Expositions Universelles*) of 1878 (*Trocadéro, Champ de Mars*), 1889 (*Eiffel Tower*), and 1900 (*Grand Palais, Petit Palais*). The *Louvre* and the *Jardin des Tuileries* also underwent changes following the fire of the *Palais des Tuileries* during the Paris Commune in 1871 (not necessarily planned changes), as well as subsequent modifications to the garden layout.

Three main types of areas account for most of the detected change: (1) areas that underwent major restructuring driven by street openings or street widenings, particularly within the *Paris Zone* (see Figure 7a); (2) infrastructure-related areas with internal evolution, such as hospitals, transport and storage facilities, and parks, where localized additions or modifications alter block-level IoU values without large-scale reconfiguration

(see Figure 7b); and (3) areas where the model fails to delineate building blocks accurately, typically due to construction lines indicating ongoing works or planned street projects (see Figure 7c).

Overall, these results reveal a heterogeneous transformation geographically, with clusters of changes concentrated in recently annexed and infrastructure-oriented areas. The central area has relatively stable spatial configuration, except for public infrastructures, parks, and major-event-driven developments. The dominant forms of detected change correspond to street openings and widenings, as well as localized reconfigurations of large infrastructures. These data-driven spatial patterns are congruent with established interpretations of Parisian urban history [40], which describe the transformation of Paris during the third republic as a continuation of the *syntax of urban improvement* that characterized the urban transformation led by Haussmann during the Second French Empire—an urban framework whose structural legacy continued to shape the evolution of Paris well into the 20th century, albeit at a noticeably slower pace. We should also note that several major undertakings of the period—such as the expansion of the Métro through extensive underground works—are scarcely visible on the change maps.

3. Discussion

3.1. Benefits of proposed framework

Detecting fine-grained change from historical maps is essential for many research fields but remains technically challenging due to severe spatial misalignments between map sheets and the often degraded graphic quality of earlier editions. Addressing these challenges requires both an alignment model capable of handling complex and non-uniform displacements, and an instance segmentation model that remains robust to stylistic variation and visual degradation. Neither aspect has been extensively explored, owing to the considerable technical complexity and the rather niche nature. In this work, we advance the state of the art on both fronts, achieving improved accuracy over existing methods. Each component—alignment and instance extraction—can also operate independently, making them broadly applicable beyond the specific pipeline presented here.

More importantly, we integrate these components into a comprehensive and highly automated framework that derives fine-grained urban change trajectories. We show its technical soundness with a case study on Paris maps, with strong validation evidence from historians and urban researchers. We also present how human intervention can be minimized within the framework. Through self-synthesis, displacement estimation can be trained in an unsupervised manner on all available data, eliminating the need for manual correspondence annotation. In fact, vector annotations of only 5% of map sheets is needed for synthesizing our cartographic knowledge for changes in objects and textual labels. Label propagation further reduces labeling effort by

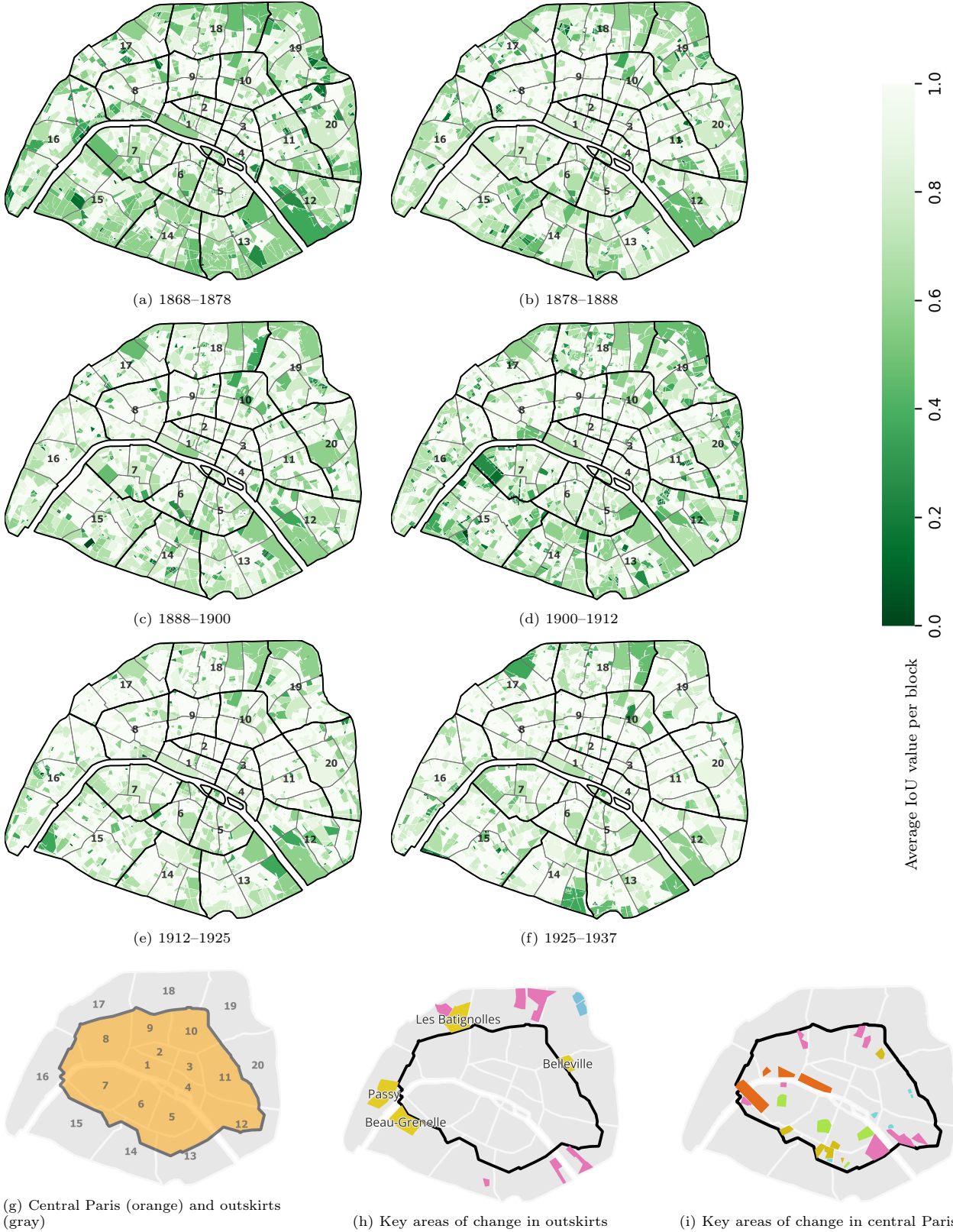


Figure 6: **Temporal change patterns of Paris from 1868–1937.** Each map covers 20 arrondissements (see (g)), subdivided into four quartiers each, for a total of 80 quartiers. Each map displays the average Intersection over Union (IoU) values per building block, calculated from the overlaps of all aligned instances within that block across two consecutive years. Lower IoU values indicate larger changes. (h) highlights areas in the outskirts associated with rail freight (pink) and waterborne freight (blue), as well as areas that remained relatively stable (yellow). (i) highlights changed areas in central Paris, including hospitals (yellow), parks (green), railway stations (pink), world exposition sites (orange), and other public buildings (blue).

Major types of detected changes



Figure 7: **Major types of changed areas and additional applications of building block representations.** Three main types of change are identified: (a) restructuring of building blocks driven by street openings and widenings; (b) infrastructure-related areas exhibiting internal modifications; and (c) apparent changes caused by false detections, typically due to construction lines indicating planned roads (blue arrow). Beyond change characterization, building block representations enable further analyses, such as street network evolution. We illustrate this by visualizing the betweenness centrality of intersections, where nodes in red correspond to the top 10% most globally connected nodes.

restricting human input to objects that actually change, reducing from approximately 70 hours to 8 hours per sheet, while map fusion leverages information from neighbouring years, requiring annotation of only a central reference sheet.

Beyond efficacy and efficiency, the proposed framework also shifts change detection on historical maps from ad hoc visual comparison to a quantitative, instance-based analysis. By using instance geometry as a proxy, our approach is robust even when maps exhibit visual discrepancies due to different production, printing, scanning, and storage conditions. The data-driven, bottom-up approach allows flexibility in how change can be conceptualized and analyzed, without imposing predefined structures. Importantly, this framework is not specific to a single city or map series, but can be derived wherever comparable historical maps are available.

3.2. Implications of fine-grained urban representations

Fine-grained urban representations derived from historical maps—including building footprints, building blocks, and their associated change profiles—provide a foundation for reference datasets capturing the long-term evolution of urban form and individually significant buildings in cities covered by large-scale historical mapping, such as London, New York, and Amsterdam. In addition, detailed building footprints and block boundaries provide a spatial framework for reconstructing street networks over time, enabling the analysis of their evolving structural roles in urban circulation. As an example, Figure 7d, Figure 7e, and Figure 7f show the temporal evolution of *betweenness centrality* at street intersections in Paris, a network measure that captures their relative importance for connectivity by quantifying how frequently they lie on shortest paths between other locations [41]. To emphasize the structural backbone of the street network, we display only locations with *betweenness centrality* values above the 90th percentile, corresponding to the top 10% most globally connected intersections. In this example, the observed evolution highlights a progressive extension of highly central nodes from the central Paris toward peripheral areas, consistent with the development of alternative circulation routes outside the city center. While similar trends have been reported for the Paris street network [42], this example illustrates how fine-grained urban block representations enable the investigation of long-term street network evolution at a finer spatial scale across successive decades.

Given the high geometric accuracy, the automatically extracted data can be corrected and validated in substantially less time, enriched with additional attributes (e.g., building names), and directly reused for a range of historical analyses, such as tracing block subdivision and consolidation or quantifying street openings and widenings. Rather than relying on visual comparison and exhaustive inspection across map editions, structured and directly comparable object representations allow experts to analyze change systematically while also able to focus on a limited set of locations—either where genuine transformations occur or where the model is likely to have failed. Finally, these detailed footprints and change trajectories are essential

for analyzing complex patterns of urban evolution and, when linked to other sources (such as professional activities, demographic data, or infrastructure investments), for studying co-evolution dynamics between the built fabric and social or economic processes.

3.3. Additional applications of map alignment

Beyond change detection within historical map series, the proposed alignment framework supports several additional analyses that rely on the same object representations and displacement estimates. In particular, the displacement fields computed during alignment constitute a valuable output in their own right. Beyond enabling object correspondence, they provide a quantitative description of geometric distortions between map editions, offering a systematic means to assess cartographic consistency, production practices, and spatial accuracy over time. Supplementary Fig. S5 shows an example of map deformations over time for *Atlas Municipal*. Applied to a single map series, these fields allow distortions to be analyzed longitudinally; applied across series, they enable comparative studies of cartographic reliability across periods or publishers.

Object-level alignment further enables the linking of individual features, such as buildings, parcels, or street segments, across temporal sequences without requiring manual correspondence annotation. This capability facilitates longitudinal analyses of urban change, supports feature-level tracking through time. In addition, alignment-derived correspondences enable label propagation across map editions, substantially reducing the need for repeated manual vectorization. An example can be found in Supplementary Fig. S7. They also provide a basis for temporal data fusion, improving robustness in sequences affected by local degradation, occlusion, or heterogeneous map quality. Together, these applications highlight how alignment outputs can be reused to support a range of analytical tasks within historical cartographic datasets, extending the utility of the framework beyond the direct detection of urban change.

3.4. Transferability to other applications

Beyond historical buildings, our workflow is readily transferable to a wide range of spatio-temporal mapping applications, especially due to its modular designs. In particular, the self-synthesis strategy used for training can be readily adapted to other object classes, such as roads, hydrographic features, vegetation, or land-use parcels, by substituting appropriate vector templates and map symbols, while requiring only limited manual annotation. This enables the generation of large-scale training data for displacement estimation across diverse mapping contexts.

Second, the alignment model is adaptable to maps with varying cartographic styles, scales, types, and projection systems, provided that the maps are geo-referenced to a common coordinate system and a small amount of vector annotation is available for self-synthesis. Supplementary Fig. S6 shows the results of

re-training our model on Siegfried maps, the topographic map series from Switzerland in the late 19th century at the scale of 1:25,000. Our model achieves robust alignment across diverse feature types, including both linear features (streams, roads, rivers, contour lines) and polygonal features (buildings), and under large displacements.

Apart from cartographic data, the framework can be applied to other forms of geospatial imagery such as aerial images. While such data is generally assumed to be well-aligned, exceptions can still happen due to varying acquisition times, sensors, viewing angles, or substantial landscape changes—for example, in post-disaster assessment or long-term environmental monitoring. In such contexts, simulating text displacement is unnecessary, while simulating geometric variation remains critical for enabling alignment models to distinguish true scene change from mis-registration. Finally, the label propagation and temporal fusion strategies supported by the framework are applicable to sequential geospatial datasets with arbitrary temporal resolution and sequence length, extending its relevance to domains such as environmental monitoring, post-disaster assessment, and long-term landscape analysis.

3.5. Limitations and potential improvements

Despite its strengths, the proposed framework has several limitations that point to directions for future work. First, the framework assumes that historical maps are geo-referenced to a common coordinate system to provide an initial coarse correspondence, which is standard practice for large-scale map archives. The current approach does not explicitly address cases where geo-referencing is missing or substantially inaccurate, and such errors may propagate to downstream alignment and change analysis. Future work could mitigate this limitation by jointly optimising geo-referencing and dense alignment within a unified framework.

Second, the alignment model is designed for topographic and cadastral maps produced under relatively consistent cartographic standards, such as those of the 19th, 20th century. Its performance may degrade for highly schematic maps or early editions characterised by extreme abstraction, non-standardised symbolisation or projection, and limited geometric consistency across years. Extending the approach to such cases will likely require incorporating higher-level semantic correspondences beyond pixel-based alignment.

Third, the current change representation treats all detected changes uniformly and does not distinguish between varying levels of importance of different objects in urban studies. Incorporating object types, functional attributes, or graded change categories could enable more nuanced analyses tailored to specific research questions and historical contexts.

4. Methods

4.1. Data

Our study utilizes historical urban planning maps from the *Atlas Municipal*, produced at the scale of 1:5000. These maps depict buildings, building blocks, and other urban infrastructures of Paris and its suburbs. Provided by the SoDuCO project (<https://soduco.geohistoricaldata.org/>), the dataset consists of 16 individual map sheets and their subsequent editions (geo-referenced), spanning 25 years between 1868 and 1937 and covering all 20 districts of Paris. Each map has approximately $10,000 \times 7,400$ pixels, with a spatial resolution of around 0.4 m/pixel. District masks are provided to crop each map, allowing a focused analysis of the central districts. To ensure spatial consistency, we rectified the geo-referenced maps depicting the same locations by converting geographical coordinates to pixel coordinates with respect to a common origin, standardizing the resolution, and cropping to a uniform spatial extent. For our analysis, we selected maps from the years 1868, 1878, 1888, 1900, 1912, 1925, and 1937 to monitor urban changes over time.

For displacement estimation, we have used the map covering the 3rd, 4th, 5th, 6th, and 7th districts for testing, while maps covering the remaining 15 districts are used for training. The maps were cropped into patches of 520×520 pixels using sliding windows, resulting in approximately 25,000 training pairs. For building instance segmentation, we manually digitized two complete map sheets and propagated their vector labels to other editions using the estimated displacement fields. After post-processing, we obtained seven annotation maps in total. We trained on sequences of three consecutive maps, each cropped into smaller patches of 512×512 pixels, yielding about 4,000 sequences for training. For testing, we randomly selected a $2,000 \times 2,000$ pixel area from two different years in each of the remaining districts and annotated them using the same label-propagation strategy.

4.2. Data synthesis

For data synthesis, we synthesize object changes, text displacements, as well as displacement between maps. The details can be seen in Supplementary Fig. S1.

Change synthesis. We randomly sample foreground objects based on the available vector annotations. Using a simple copy-and-paste method [43], we generate a modified copy from the original image under four scenarios: “addition” if the foreground objects are pasted in the copy, “deletion” if the foreground objects are pasted in the original image, “replacement” if both addition and deletion happen, and “unchanged” if no foreground objects are used. This setup enables the model to learn from diverse types of object changes.

Text-displacement synthesis. To extract textual elements, we borrow the off-the-shelf state-of-art text detection model DeepSolo [44] based on the transformer architecture. We fine-tune it on the open dataset

ICDAR 2024 Competition for Historical Map Text Detection, Recognition, and Linking [45]. Similarly, we use the copy-and-paste strategy to simulate random text displacements on both the original image and its copy, and integrate these perturbations with the change synthesis process.

Displacement synthesis. To simulate realistic geometric distortions, we apply a range of transformations—including homography, affine, thin plate splines (TPS), and their combinations [46]—to the copied image. The corresponding ground-truth displacement fields are then used to supervise the model. To increase robustness to appearance variations, we randomly adjust brightness, saturation, and contrast while keeping hue unchanged, as hue often encodes semantic class information in maps (e.g., hydrological features are typically blue). We also apply subtle Gaussian blurs to introduce minor texture variations, further enhancing the model’s resilience to visual inconsistencies.

4.3. Displacement estimation

Problem definition. Given two map patches $I \in \mathbb{R}^{H \times W \times 3}$ and $J \in \mathbb{R}^{H \times W \times 3}$ depicting the same area of the same size $H \times W$, our goal is to estimate pixel-wise displacements that are pixel-wise 2D motion vectors, $F_{I \rightarrow J} \in \mathbb{R}^{H \times W \times 2}$, often also denoted as optical flow, in the coordinate system of image I , that relates pixels in I to J .

Triplet consistency. Given a real image pair I, J , we construct an image triplet comprised of I, J , and I' , with I' being a synthesized copy of I augmented with synthesized changes, randomly displaced texts, and a known displacement field W . The displacement consistency along the triplet between W and the composition from $I' \rightarrow J \rightarrow I$ can be modeled:

$$W = \hat{F}_{I' \rightarrow J} + \phi_{\hat{F}_{I' \rightarrow J}}(\hat{F}_{J \rightarrow I}), \quad (1)$$

where $\hat{F}_{I' \rightarrow J}$ is the estimated displacement from I' to J and $\hat{F}_{J \rightarrow I}$ is the estimated displacement from J to I . $\phi_{\hat{F}_{I' \rightarrow J}}$ warps the $\hat{F}_{J \rightarrow I}$ in the coordinate system of J into that of I' , to align with $\hat{F}_{I' \rightarrow J}$. This consistency is used to refine the displacement estimation $\hat{F}_{I' \rightarrow J}$ and $\hat{F}_{J \rightarrow I}$. The consistency is enforced only in valid regions where pixels from both sides represent a valid, non-occluded mapping and do not fall outside the image boundaries [29].

Network structure. Given the triplet formed by I, J and the modified copy I' , following WarpC [29], we use GLU-Net [27] for displacement estimation between each pair $\hat{F}_{I' \rightarrow J}$, $\hat{F}_{J \rightarrow I}$ and $\hat{F}_{I' \rightarrow I}$ with shared parameters θ . The architecture of GLU-Net can be found in Supplementary Fig. S2. It estimates the displacement fields through a hierarchical workflow, which can capture and align multi-scale details. The feature extractor extracts four levels of image features in total. At each feature level, the correlation between the extracted features from the paired inputs is computed and used to estimate the displacement field at this resolution.

Loss. In the constructed triplet (I, J, I') , the ground-truth displacement W between I' and I is known at the original resolution $H \times W$. We can obtain the direct supervision loss:

$$\mathcal{L}_{I' \rightarrow I} = \sum_l \alpha^l \|\hat{F}_{I' \rightarrow I}^l - W^l\|, \quad (2)$$

where l indicates the feature level and α^l is the scalar factor to weight the loss at this level. W is down-sampled it to $H_l \times W_l$ each level l to calculate the multi-level loss. According to the equation (1), we can enforce the consistency between the composition flow $I \rightarrow J \rightarrow I'$ and the known flow $I' \rightarrow I$ at multiple levels:

$$\mathcal{L}_{I' \rightarrow J \rightarrow I} = \sum_l \alpha^l \|\hat{F}_{I' \rightarrow J}^l + \phi_{\hat{F}_{I' \rightarrow J}^l}(\hat{F}_{J \rightarrow I}^l) - W^l\|. \quad (3)$$

By combining equations (2) and (6), we have the overall objective:

$$\mathcal{L} = \sum_{(I, I')} \mathcal{L}_{I' \rightarrow I} + \sum_{(I, I', J)} \mathcal{L}_{I' \rightarrow J \rightarrow I}. \quad (4)$$

4.4. Instance extraction

In our work, we adapt Mask2Former [38] for segmenting building instances, a state-of-the-art architecture suitable for both semantic and instance segmentation based on the transformer architecture [47]. Compared with CNNs, transformers handle long-range context by modeling the global relationship between all locations based on the self-attention mechanism [47] and have shown remarkable improvements in image segmentation [48, 38]. We argue that the long-range context is especially advantageous for segmenting our maps, where most building instances are represented as polygons without any textures. Rather than segmentation per pixel, Mask2Former uses mask classification that groups pixels into N segments as N binary masks. Each mask is assigned both an instance label and a corresponding class category label. These masks guide the transformer’s attention to focus on features within the masked region, thereby improving training efficiency. In our case, we define two classes—roads and building units, the latter defined as closed-shape polygons. The model outputs a predicted class and instance ID for each pixel.

To overcome degrading graphic quality, we add multi-scale feature fusion blocks given features from different years. Our modified architecture is illustrated in Supplementary Fig. S3. Following the original architecture, given a sequence of images, our model has a shared backbone to extract image features, a shared pixel decoder to restore the original image resolution from the backbone features, and a transformer decoder that predicts the instance mask and class from the multi-level pixel features. To fuse the features from different images at each feature level, we use the cross-attention module, followed by a Feed Forward

Algorithm 1: Stitching Instance Predictions

```
1 Algorithm parameters: patches_images  $P$ , patch_size  $s$ , step_size  $t$ , image_height  $h$ ,  
image_width  $w$ , overlap  $o$ ;  
2 Initialize: output image  $I$  as empty, rows  $r \leftarrow h/t - 1$ , cols  $c \leftarrow w/t - 1$ ,  $global_id \leftarrow 0$ ;  
3 for  $i$  in  $r$  do  
4   for  $j$  in  $c$  do  
5     Extract the current patch  $p \leftarrow P[i + cj]$   
6     Identify unique instance IDs ( $id$ )  
7     Extract the overlapped regions from the upper tile  $i^u \leftarrow I[i * t : i * t + o, j * t : i * t + s]$   
8     Extract the overlapped regions from the left tile  $i^l \leftarrow I[i * t : i * t + s, j * t : i * t + o]$   
9     for  $id$  do  
10       Get the best IoU of  $p_{id}$  and all instances in  $i^u$  and obtain the corresponding ID  $id^u$   
11       if  $best\ IoU > 0$  then  
12          $id \leftarrow id^u$   
13       else  
14         Get the best IoU of  $p_{id}$  and all instances in  $i^l$  and obtain the corresponding ID  $id^l$   
15         if  $best\ IoU > 0$  then  
16            $id \leftarrow id^l$   
17         else  
18            $id \leftarrow global_id$   
19            $global_id \leftarrow global_id + 1$   
20    $I[i + cj] \leftarrow p$   
21 return  $I$ 
```

Network (FFN), which is comprised of two linear transformations with ReLU activation and dropouts in between. Note that we apply the estimated displacement fields to spatially align the map editions beforehand to ensure better feature correspondences at the same location across years.

At inference, the maps are cropped into tiles of 512×512 pixels with 50% overlap and the model generates predictions for each tile. To reconstruct complete instances across the entire map sheet, we identify the same instance across overlapping tiles and unify the instance ID. The corresponding pseudo-code is presented below. For each tile, instances are compared with those in the overlapping regions of the adjacent tiles—specifically, the tile directly above and the tile to the right. The Intersection over Union (IoU) is calculated for each pair of instances. The ID of the overlapping instance with the highest IoU (greater than 0) is assigned to the current instance. To prevent duplicated assignments, this process is performed for either the tile above or the tile to the right, but not both simultaneously.

4.5. Evaluation metrics

Displacement smoothness. We measure the smoothness of the displacement field using mean variation (mV). It calculates the average of the absolute gradient between neighboring pixels:

$$mV = \frac{1}{N} \sum_{(x,y) \in \Omega} \sum_{(i,j) \in \mathcal{N}} \|\mathbf{u}(x,y) - \mathbf{u}(x+i,y+j)\|_1, \quad (5)$$

where $\mathbf{u}(x,y)$ is a displacement vector at the position (x,y) . N is the number of pixels, and \mathcal{N} is a set of neighbor offsets, e.g., $\{(1,0), (0,1), (-1,0), (0,-1)\}$ for 4-neighborhood.

Displacement consistency. Similar to Equation (6), we evaluate the L1 consistency of the displacement estimation within a triplet from three consecutive years T_1, T_2, T_3 :

$$L1 = \|\widehat{F}_{T_1 \rightarrow T_2} + \phi_{\widehat{F}_{T_1 \rightarrow T_2}}(\widehat{F}_{T_2 \rightarrow T_3}) - \widehat{F}_{T_1 \rightarrow T_3}\|. \quad (6)$$

Image-level comparison. We use the the structural similarity index (SSIM) to measure the image similarity:

$$SSIM = \frac{(2\mu_x\mu_y + c_1)(2\sigma_{xy} + c_2)}{(\mu_x^2 + \mu_y^2 + c_1)(\sigma_x^2 + \sigma_y^2 + c_2)}, \quad (7)$$

where μ_x and μ_y are average values; σ_x and σ_y are variances; σ_{xy} is the covariance of x and y; $c_1 = (k_1 L)^2$ and $c_2 = (k_2 L)^2$ are constants with $k_1 = 0.01$, $k_2 = 0.03$ and L being the dynamic range of the image pixel values. For RGB images, the per-channel RMSE and SSIM are calculated and averaged.

Object-level comparison. We use Chamfer distance (CD) to measure the average shortest distance between objects from two sets. CD between the two point sets S_1 and S_2 is defined as:

$$CD = \frac{1}{|S_1|} \sum_{x \in S_1} \min_{y \in S_2} \|x - y\|^2 + \frac{1}{|S_2|} \sum_{y \in S_2} \min_{x \in S_1} \|y - x\|^2. \quad (8)$$

Each point $x \in S_1$ finds its closest neighbor in S_2 and vice versa. All point-wise distances are averaged. In our case, CD measures the distance between the sets of vertices filtered by the specific distance threshold.

Instance-level comparison. The average precision (AP) [49] score is normally used to evaluate the accuracy for instance segmentation. It's based on the precision and the recall score. The Hungarian matching [50] is used to assign a one-to-one matching between predicted instances and the ground truth as a standard approach. A predicted instance is considered correct if its Intersection over Union (IoU) with the matched ground-truth instance exceeds a predefined threshold θ . Precision measures how many of the predicted instances are correct, while recall measures how many of the ground-truth instances are correctly detected.

$$Precision = \frac{TP}{TP + FP}, \quad (9)$$

$$Recall = \frac{TP}{TP + FN}, \quad (10)$$

And the AP is the area under the precision-recall curve (AUC):

$$AP = \int_0^1 p(r)dr, \quad (11)$$

where p is the precision at recall r , computed at a certain IoU threshold θ , typically larger than 0.5. In practice, this is calculated using discrete values by averaging precision across all recall levels [51, 52, 53].

References

- [1] S. Chakraborty, H. Dadashpoor, J. Novotný, I. Maity, A. Follmann, P. P. Patel, U. Roy, S. Pramanik, In pursuit of sustainability–spatio-temporal pathways of urban growth patterns in the world’s largest megacities, *Cities* 131 (2022) 103919.
- [2] C. Wu, C. Li, L. Ouyang, H. Xiao, J. Wu, M. Zhuang, X. Bi, J. Li, C. Wang, C. Song, et al., Spatiotemporal evolution of urbanization and its implications to urban planning of the megacity, shanghai, china, *Landscape Ecology* 38 (4) (2023) 1105–1124.
- [3] X. Liu, Y. Huang, X. Xu, X. Li, X. Li, P. Ciais, P. Lin, K. Gong, A. D. Ziegler, A. Chen, et al., High-spatiotemporal-resolution mapping of global urban change from 1985 to 2015, *Nature Sustainability* 3 (7) (2020) 564–570.
- [4] J. Yang, X. Huang, 30 m annual land cover and its dynamics in china from 1990 to 2019, *Earth System Science Data Discussions* 2021 (2021) 1–29.
- [5] X. Huang, J. Li, J. Yang, Z. Zhang, D. Li, X. Liu, 30 m global impervious surface area dynamics and urban expansion pattern observed by landsat satellites: From 1972 to 2019, *Science China Earth Sciences* 64 (2021) 1922–1933.
- [6] H. Chen, Z. Shi, A spatial-temporal attention-based method and a new dataset for remote sensing image change detection, *Remote Sensing* 12 (10) (2020).
- [7] A. Geiger, P. Lenz, C. Stiller, R. Urtasun, Vision meets robotics: The kitti dataset, *The international journal of robotics research* 32 (11) (2013) 1231–1237.

[8] C. San-Antonio-Gómez, C. Velilla, F. Manzano-Agugliaro, Urban and landscape changes through historical maps: The Real Sitio of Aranjuez (1775–2005), a case study, *Computers, Environment and Urban Systems* 44 (2014) 47–58. [doi:10.1016/j.compenvurbsys.2013.12.001](https://doi.org/10.1016/j.compenvurbsys.2013.12.001).

[9] K. Burghardt, J. H. Uhl, K. Lerman, S. Leyk, Road network evolution in the urban and rural United States since 1900, *Computers, Environment and Urban Systems* 95 (2022) 101803.

[10] D. Tonolla, M. Geilhausen, M. Doering, Seven decades of hydrogeomorphological changes in a near-natural (Sense River) and a hydropower-regulated (Sarine River) pre-Alpine river floodplain in Western Switzerland, *Earth Surface Processes and Landforms* 46 (1) (2021) 252–266. [doi:10.1002/esp.5017](https://doi.org/10.1002/esp.5017).

[11] P. Picuno, G. Cillis, D. Statuto, Investigating the time evolution of a rural landscape: How historical maps may provide environmental information when processed using a GIS, *Ecological Engineering* 139 (2019) 105580. [doi:10.1016/j.ecoleng.2019.08.010](https://doi.org/10.1016/j.ecoleng.2019.08.010).

[12] Y. M. Räth, A. Grêt-Regamey, C. Jiao, S. Wu, M. J. van Strien, Settlement relationships and their morphological homogeneity across time and scale, *Scientific Reports* 13 (1) (2023) 11248.

[13] S. Wu, M. Heitzler, L. Hurni, Leveraging uncertainty estimation and spatial pyramid pooling for extracting hydrological features from scanned historical topographic maps, *GIScience & Remote Sensing* 59 (1) (2022) 200–214.

[14] Y. Chen, J. Chazalon, E. Carlinet, M. Ôn Vñ Ngoc, C. Mallet, J. Perret, Automatic vectorization of historical maps: A benchmark, *Plos one* 19 (2) (2024) e0298217.

[15] S. Wu, K. Schindler, M. Heitzler, L. Hurni, Domain adaptation in segmenting historical maps: A weakly supervised approach through spatial co-occurrence, *ISPRS Journal of Photogrammetry and Remote Sensing* 197 (2023) 199–211.

[16] M. Heitzler, L. Hurni, Cartographic reconstruction of building footprints from historical maps: A study on the Swiss Siegfried map, *Transactions in GIS* 24 (2) (2020) 442–461.

[17] J. H. Uhl, S. Leyk, Y.-Y. Chiang, W. Duan, C. A. Knoblock, Automated extraction of human settlement patterns from historical topographic map series using weakly supervised convolutional neural networks, *IEEE Access* 8 (2019) 6978–6996.

[18] S. Wu, R. Schnürer, M. Heitzler, L. Hurni, Unsupervised historical map registration by a deformation neural network, in: *Proceedings of the 5th ACM SIGSPATIAL International Workshop on AI for Geographic Knowledge Discovery*, 2022, pp. 76–81.

[19] R. C. Daudt, B. Le Saux, A. Boulch, Fully convolutional siamese networks for change detection, in: 2018 25th IEEE international conference on image processing (ICIP), IEEE, 2018, pp. 4063–4067.

[20] D. Peng, Y. Zhang, H. Guan, End-to-end change detection for high resolution satellite images using improved unet++, *Remote Sensing* 11 (11) (2019) 1382.

[21] H. Chen, Z. Qi, Z. Shi, Remote sensing image change detection with transformers, *IEEE Transactions on Geoscience and Remote Sensing* 60 (2021) 1–14.

[22] S. Fang, K. Li, J. Shao, Z. Li, Snunet-cd: A densely connected siamese network for change detection of vhr images, *IEEE Geoscience and Remote Sensing Letters* 19 (2022) 1–5.

[23] C. Zhang, P. Yue, D. Tapete, L. Jiang, B. Shangguan, L. Huang, G. Liu, A deeply supervised image fusion network for change detection in high resolution bi-temporal remote sensing images, *ISPRS Journal of Photogrammetry and Remote Sensing* 166 (2020) 183–200.

[24] Z. Hou, Y. Qu, L. Zhang, J. Liu, F. Wang, Q. Yu, A. Zeng, Z. Chen, Y. Zhao, H. Tang, et al., War city profiles drawn from satellite images, *Nature Cities* (2024) 1–11.

[25] X. Shen, F. Darmon, A. A. Efros, M. Aubry, Ransac-flow: generic two-stage image alignment, in: Computer Vision–ECCV 2020: 16th European Conference, Glasgow, UK, August 23–28, 2020, Proceedings, Part IV 16, Springer, 2020, pp. 618–637.

[26] I. Melekhov, A. Tiulpin, T. Sattler, M. Pollefeys, E. Rahtu, J. Kannala, Dgc-net: Dense geometric correspondence network, in: 2019 IEEE Winter Conference on Applications of Computer Vision (WACV), IEEE, 2019, pp. 1034–1042.

[27] P. Truong, M. Danelljan, R. Timofte, Glu-net: Global-local universal network for dense flow and correspondences, in: Proceedings of the IEEE/CVF conference on computer vision and pattern recognition, 2020, pp. 6258–6268.

[28] P. Truong, M. Danelljan, R. Timofte, L. Van Gool, Pdc-net+: Enhanced probabilistic dense correspondence network, *IEEE Transactions on Pattern Analysis and Machine Intelligence* (2023).

[29] P. Truong, M. Danelljan, F. Yu, L. Van Gool, Warp consistency for unsupervised learning of dense correspondences, in: Proceedings of the IEEE/CVF International Conference on Computer Vision, 2021, pp. 10346–10356.

[30] J.-M. Park, U.-H. Kim, S.-H. Lee, J.-H. Kim, Dual task learning by leveraging both dense correspondence and mis-correspondence for robust change detection with imperfect matches, in: 2022 IEEE Conference on Computer Vision and Pattern Recognition, CVPR 2022, 2022.

[31] S. Baker, D. Scharstein, J. Lewis, S. Roth, M. J. Black, R. Szeliski, A database and evaluation methodology for optical flow, *International journal of computer vision* 92 (2011) 1–31.

[32] J. Hur, S. Roth, Optical flow estimation in the deep learning age, *Modelling Human Motion: From Human Perception to Robot Design* (2020) 119–140.

[33] A. Dosovitskiy, P. Fischer, E. Ilg, P. Hausser, C. Hazirbas, V. Golkov, P. Van Der Smagt, D. Cremers, T. Brox, Flownet: Learning optical flow with convolutional networks, in: *Proceedings of the IEEE international conference on computer vision*, 2015, pp. 2758–2766.

[34] D. Sun, X. Yang, M.-Y. Liu, J. Kautz, Pwc-net: Cnns for optical flow using pyramid, warping, and cost volume, in: *Proceedings of the IEEE conference on computer vision and pattern recognition*, 2018, pp. 8934–8943.

[35] D. Sun, X. Yang, M.-Y. Liu, J. Kautz, Models matter, so does training: An empirical study of cnns for optical flow estimation, *IEEE transactions on pattern analysis and machine intelligence* 42 (6) (2019) 1408–1423.

[36] T.-W. Hui, X. Tang, C. C. Loy, Liteflownet: A lightweight convolutional neural network for optical flow estimation, in: *Proceedings of the IEEE conference on computer vision and pattern recognition*, 2018, pp. 8981–8989.

[37] S. Wu, Y. Chen, K. Schindler, L. Hurni, Cross-attention spatio-temporal context transformer for semantic segmentation of historical maps, in: *Proceedings of the 31st ACM International Conference on Advances in Geographic Information Systems*, 2023, pp. 1–9.

[38] B. Cheng, I. Misra, A. G. Schwing, A. Kirillov, R. Girdhar, Masked-attention mask transformer for universal image segmentation, 2022.

[39] J. Cannon, *The Paris zone: A cultural history, 1840-1944*, Routledge, 2016.

[40] C. Jones, *Paris: biography of a city*, Penguin UK, 2006.

[41] L. C. Freeman, A set of measures of centrality based on betweenness, *Sociometry* 40 (1) (1977) 35–41.

[42] A. Kirkley, H. Barbosa, M. Barthelemy, G. Ghoshal, From the betweenness centrality in street networks to structural invariants in random planar graphs, *Nature communications* 9 (1) (2018) 2501.

[43] D. Dwibedi, I. Misra, M. Hebert, Cut, paste and learn: Surprisingly easy synthesis for instance detection, in: Proceedings of the IEEE international conference on computer vision, 2017, pp. 1301–1310.

[44] M. Ye, J. Zhang, S. Zhao, J. Liu, T. Liu, B. Du, D. Tao, Deep solo: Let transformer decoder with explicit points solo for text spotting, in: Proceedings of the IEEE/CVF Conference on Computer Vision and Pattern Recognition (CVPR), 2023, pp. 19348–19357.

[45] Z. Li, Y. Lin, Y.-Y. Chiang, J. Weinman, S. Tual, J. Chazalon, J. Perret, B. Duménieu, N. Abadie, Icdar 2024 competition on historical map text detection, recognition, and linking, in: International Conference on Document Analysis and Recognition, Springer, 2024, pp. 363–380.

[46] I. Rocco, R. Arandjelovic, J. Sivic, Convolutional neural network architecture for geometric matching, in: Proceedings of the IEEE conference on computer vision and pattern recognition, 2017, pp. 6148–6157.

[47] A. Vaswani, Attention is all you need, *Advances in Neural Information Processing Systems* (2017).

[48] B. Cheng, A. G. Schwing, A. Kirillov, Per-pixel classification is not all you need for semantic segmentation, in: *Advances in neural information processing systems*, 2021, pp. 17864–17875.

[49] T.-Y. Lin, M. Maire, S. Belongie, J. Hays, P. Perona, D. Ramanan, P. Dollár, C. L. Zitnick, Microsoft coco: Common objects in context, in: European conference on computer vision (ECCV), Springer, 2014, pp. 740–755.

[50] N. Carion, F. Massa, G. Synnaeve, N. Usunier, A. Kirillov, S. Zagoruyko, End-to-end object detection with transformers, in: European conference on computer vision, Springer, 2020, pp. 213–229.

[51] M. Everingham, L. Van Gool, C. K. I. Williams, J. Winn, A. Zisserman, [The pascal visual object classes challenge 2012 \(voc2012\) results](#) (2012).

URL <http://www.pascal-network.org/challenges/VOC/voc2012/workshop/index.html>

[52] [Coco detection challenge \(bounding box\)](#) (2019).

URL <https://competitions.codalab.org/competitions/20794>

[53] R. Padilla, W. L. Passos, T. L. B. Dias, S. L. Netto, E. A. B. da Silva, A comparative analysis of object detection metrics with a companion open-source toolkit, *Electronics* 10 (3) (2021).

[54] D. G. Lowe, Distinctive image features from scale-invariant keypoints, *International journal of computer vision* 60 (2004) 91–110.

[55] H. Bay, T. Tuytelaars, L. Van Gool, Surf: Speeded up robust features, in: Computer Vision–ECCV 2006: 9th European Conference on Computer Vision, Graz, Austria, May 7-13, 2006. Proceedings, Part I 9, Springer, 2006, pp. 404–417.

[56] E. Rublee, V. Rabaud, K. Konolige, G. Bradski, Orb: An efficient alternative to sift or surf, in: 2011 International conference on computer vision, Ieee, 2011, pp. 2564–2571.

[57] P. Truong, S. Apostolopoulos, A. Mosinska, S. Stucky, C. Ciller, S. D. Zanet, Glampoints: Greedily learned accurate match points, in: Proceedings of the IEEE/CVF International Conference on Computer Vision, 2019, pp. 10732–10741.

[58] K. M. Yi, E. Trulls, V. Lepetit, P. Fua, Lift: Learned invariant feature transform, in: Computer Vision–ECCV 2016: 14th European Conference, Amsterdam, The Netherlands, October 11-14, 2016, Proceedings, Part VI 14, Springer, 2016, pp. 467–483.

[59] D. DeTone, T. Malisiewicz, A. Rabinovich, Superpoint: Self-supervised interest point detection and description, in: Proceedings of the IEEE conference on computer vision and pattern recognition workshops, 2018, pp. 224–236.

[60] Y. Ono, E. Trulls, P. Fua, K. M. Yi, Lf-net: Learning local features from images, Advances in neural information processing systems 31 (2018).

[61] R. Szeliski, et al., Image alignment and stitching: A tutorial, Foundations and Trends® in Computer Graphics and Vision 2 (1) (2007) 1–104.

[62] J.-M. Park, U.-H. Kim, S.-H. Lee, J.-H. Kim, Dual task learning by leveraging both dense correspondence and mis-correspondence for robust change detection with imperfect matches, in: Proceedings of the IEEE/CVF Conference on Computer Vision and Pattern Recognition, 2022, pp. 13749–13759.

[63] N. Mayer, E. Ilg, P. Hausser, P. Fischer, D. Cremers, A. Dosovitskiy, T. Brox, A large dataset to train convolutional networks for disparity, optical flow, and scene flow estimation, in: Proceedings of the IEEE conference on computer vision and pattern recognition, 2016, pp. 4040–4048.

[64] Z. Ren, J. Yan, B. Ni, B. Liu, X. Yang, H. Zha, Unsupervised deep learning for optical flow estimation, in: Proceedings of the AAAI conference on artificial intelligence, Vol. 31, 2017.

[65] R. Jonschkowski, A. Stone, J. T. Barron, A. Gordon, K. Konolige, A. Angelova, What matters in unsupervised optical flow, in: Computer Vision–ECCV 2020: 16th European Conference, Glasgow, UK, August 23–28, 2020, Proceedings, Part II 16, Springer, 2020, pp. 557–572.

[66] L. Barazzetti, R. Brumana, D. Oreni, M. Previtali, Historical map registration via independent model adjustment with affine transformations, in: Computational Science and Its Applications (ICCSA), Springer, 2014, pp. 44–56.

[67] B. Vaienti, I. Di Lenardo, F. Kaplan, Exploring cartographic genealogies through deformation analysis: case studies on ancient maps and synthetic data, *Cartography and Geographic Information Science* 52 (5) (2025) 557–577.

[68] B. Vaienti, I. di Lenardo, F. Kaplan, Georeferencing historical maps using local feature matching and Delaunay consistency, *Cartography and Geographic Information Science* (2025). [doi:10.1080/15230406.2025.2566789](https://doi.org/10.1080/15230406.2025.2566789).

[69] J. Deng, X. Chen, D. Zhang, Automatic evaluation and optimization of map registration based on feature overlap area ratio, *Geocarto International* 39 (1) (2024) 2359481.

[70] S. Zambanini, Feature-based groupwise registration of historical aerial images to present-day ortho-photo maps, *Pattern Recognition* 90 (2019) 66–77.

[71] J. Luft, J. Schiewe, Automatic content-based georeferencing of historical topographic maps, *Transactions in GIS* 25 (6) (2021) 2888–2906.

[72] J. Luft, J. Schiewe, Content-based Image Retrieval for Map Georeferencing, *Proceedings of the ICA* 4 (2021) 69.

[73] W. Y. Yan, S. M. Easa, A. Shaker, Polygon-based image registration: A new approach for geo-referencing historical maps, *Remote Sensing Letters* 8 (7) (2017) 703–712.

[74] K. Sun, Y. Hu, J. Song, Y. Zhu, Aligning geographic entities from historical maps for building knowledge graphs, *International Journal of Geographical Information Science* 35 (10) (2021) 2078–2107.

[75] D. Bin, W. K. Cheong, A system for automatic extraction of road network from maps, in: International Joint Symposia on Intelligence and Systems, 1998, pp. 359–366.

[76] D. B. Dhar, B. Chanda, Extraction and recognition of geographical features from paper maps, *International Journal of Document Analysis and Recognition (IJDAR)* 8 (2006) 232–245.

[77] S. Leyk, Segmentation of colour layers in historical maps based on hierarchical colour sampling, in: *Proceedings of the IAPR International Workshop on Graphics Recognition (GREC)*, Springer, 2010, pp. 231–241.

[78] A. Khotanzad, E. Zink, Contour line and geographic feature extraction from usgs color topographical paper maps, *IEEE Transactions on Pattern Analysis and Machine Intelligence* 25 (1) (2003) 18–31.

[79] R. Samet, E. Hancer, A new approach to the reconstruction of contour lines extracted from topographic maps, *Journal of Visual Communication and Image Representation* 23 (4) (2012) 642–647.

[80] Y.-Y. Chiang, S. Leyk, C. A. Knoblock, Efficient and robust graphics recognition from historical maps, in: *Graphics Recognition. New Trends and Challenges: 9th International Workshop, GREC 2011, Seoul, Korea, September 15-16, 2011, Revised Selected Papers*, Springer, 2013, pp. 25–35.

[81] B. Ekim, E. Sertel, M. E. Kabadayı, Automatic road extraction from historical maps using deep learning techniques: A regional case study of turkey in a german world war ii map, *ISPRS International Journal of Geo-Information* 10 (8) (2021) 492.

[82] C. Jiao, Extracting road features from historical maps by incorporating cartographic method knowledge into deep learning, Ph.D. thesis, ETH Zurich (2024).

[83] Y. Chen, E. Carlinet, J. Chazalon, C. Mallet, B. Duménieu, J. Perret, Combining deep learning and mathematical morphology for historical map segmentation, in: *International Conference on Discrete Geometry and Mathematical Morphology*, Springer, 2021, pp. 79–92.

[84] S. Wu, M. Heitzler, L. Hurni, a closer look at segmentation uncertainty of scanned historical maps, *International Archives of the Photogrammetry, Remote Sensing and Spatial Information Sciences (ISPRS Archives)* 43 (2022) 189–194.

[85] R. O'Hara, R. Marwaha, J. Zimmerman, M. Saunders, S. Green, Unleashing the power of old maps: Extracting symbology from nineteenth century maps using convolutional neural networks to quantify modern land use on historic wetlands, *Ecological Indicators* 158 (2024) 111363.

[86] Z. Li, R. Guan, Q. Yu, Y.-Y. Chiang, C. A. Knoblock, Synthetic map generation to provide unlimited training data for historical map text detection, in: *Proceedings of the ACM SIGSPATIAL International Workshop on AI for Geographic Knowledge Discovery*, 2021, pp. 17–26.

[87] Y. Lin, Y.-Y. Chiang, Hyper-local deformable transformers for text spotting on historical maps, in: *Proceedings of the ACM SIGKDD Conference on Knowledge Discovery and Data Mining*, 2024, pp. 5387–5397.

[88] Y. Chen, E. Carlinet, J. Chazalon, C. Mallet, B. Duménieu, J. Perret, Vectorization of historical maps using deep edge filtering and closed shape extraction, in: *International conference on document analysis and recognition*, Springer, 2021, pp. 510–525.

Supplementary Note 1: Technical terms

Geo-referencing. Geo-referencing is the process of associating spatial data (such as maps, aerial images, or satellite photos) with specific geographic coordinates in a particular coordinate system.

Image rectification. Image rectification refers to applying a geometric transformation to align images to a common reference frame. In this paper, it specifically denotes transforming images so that they share the same origin, spatial resolution, and image size.

Image matching. Image matching is a fundamental computer vision problem that aims to find correspondences between image pairs.

Map cropping. Map cropping is the process of partitioning a large map sheet, which is often too large to process directly, into smaller patches such as 256×256 pixels.

Displacement estimation. Displacement estimation is the process of estimating a pixel-wise displacement field between two images by computing the shift vectors of corresponding pixels, enabling image alignment.

Warping. Warping is the process of geometrically transforming a source image by shifting its pixels according to a displacement field so that they align with corresponding positions in a target image.

Vector annotation. Vector annotation refers to the process of manually or semi-automatically labeling map features such as buildings, roads, or rivers, by annotating them as vector geometries such as points, lines, or polygons.

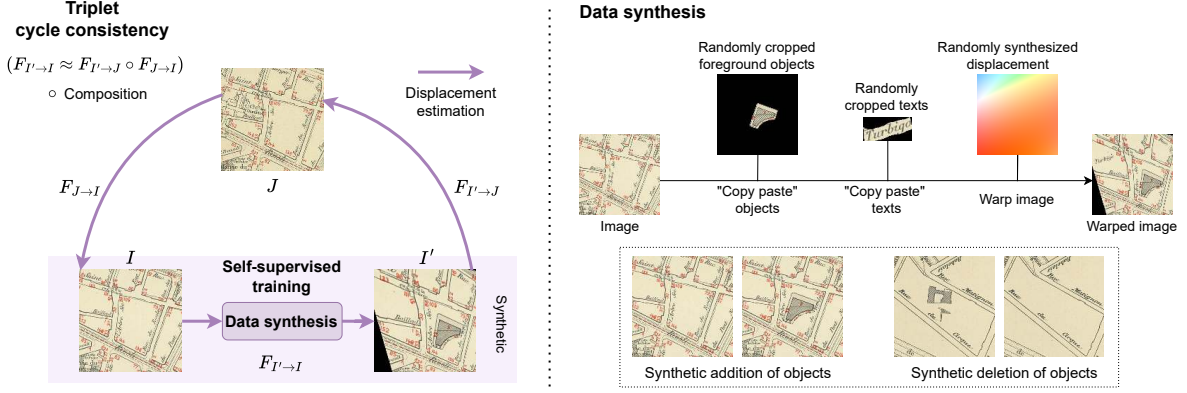
Label propagation. Label propagation refers to assigning labels to unlabeled pixels or regions by propagating known labels through spatial or temporal relationships. In this paper, it refers to propagating labels across maps from different years.

Instance segmentation. Instance segmentation is the task of simultaneously performing object detection and pixel-wise segmentation, such that each object instance is segmented and assigned a unique instance ID.

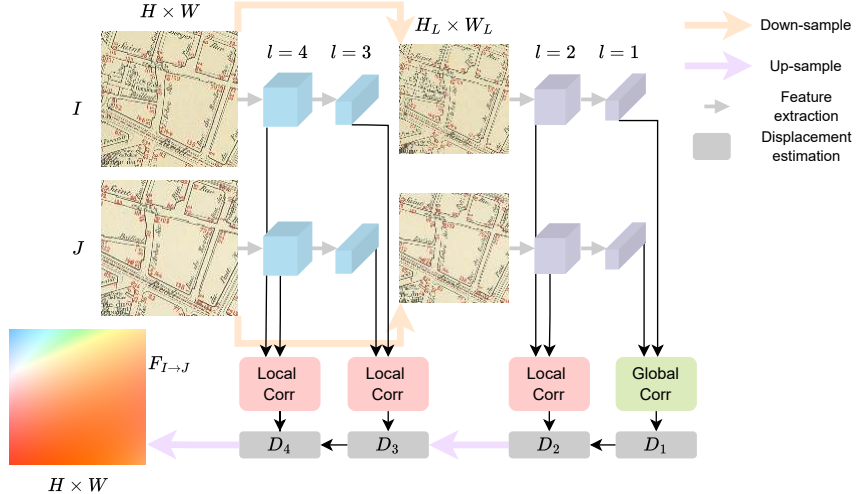
Cross attention. Cross attention is an attention mechanism where the query and the key–value pairs are derived from different feature sets, enabling one representation to selectively attend to and integrate information from another.

Supplementary Note 2: More details of methodology

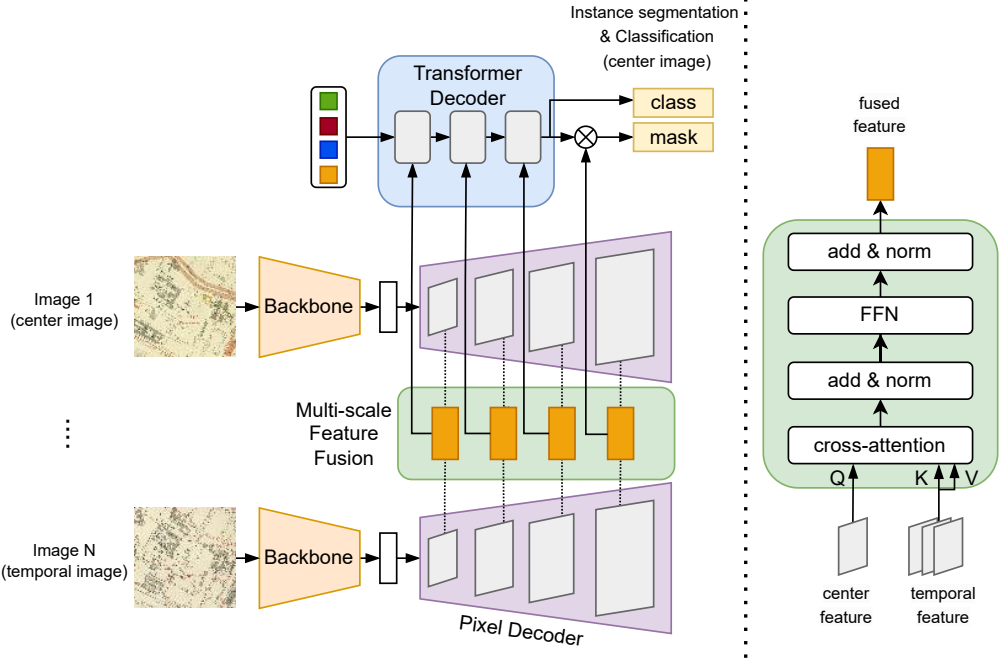
Details of triplet cycle consistency, data synthesis, the displacement estimation network and instance segmentation network.



Supplementary Fig. S1: Detailed illustration of triplet cycle consistency and self-supervised data synthesis used for displacement estimation. Images are synthesized with known displacements, with random text and object injections to train the network to ignore these disturbances.



Supplementary Fig. S2: For displacement estimation, we use the GLU-Net architecture [27]. The paired images I , J are first down-sampled. Both original and down-sampled images are fed into feature extractors, resulting in multi-level features. Local and global correlations between the source and target features are computed at multiple levels $l \in \{1, 2, 3, 4\}$. Using these correlations, multi-level displacement fields are iteratively estimated by refining the displacement from the previous level with the current correlation information. The estimated displacement field from the final layer is up-sampled to produce the final estimation.



Supplementary Fig. S3: Our proposed architecture for instance segmentation. We extend the Mask2former model by introducing multi-scale feature fusion blocks to integrate features from maps at different years, based on the cross-attention mechanism. Note that we apply the estimated displacement fields to spatially align the map editions across years beforehand.

Supplementary Note 3: Experiment details

For displacement estimation, we trained our model with a batch size of 12 on NVIDIA RTX 3090 GPU. We used the Adam Optimizer with a learning rate of 1e-4 and a weight decay of 4e-4. Given the substantial size of our dataset (25,000 pairs), the model was trained for 20 epochs, where convergence was observed. For instance segmentation, we trained our model with a batch size of 4 on NVIDIA RTX 4090 GPU. We used the Adam optimizer with a learning rate of 5e-5 and we trained the model for 25 epochs, given the dataset of 4,000 sequences, each consisting 3 images.

Supplementary Note 4: Related work

.1 Image matching

Image matching can be classified into sparse and dense matching. Sparse matching methods rely on detecting stable, representative, repeatable, and sparse key points across images [54, 55, 56, 57, 58, 59, 60]. Typically, local image features from key points are matched to estimate the geometric transformation (e.g. affine or homography) between images [61]. On the other hand, dense matching estimates the per-pixel correspondence and displacement between images, especially with the help of deep learning methods. It has mostly been addressed in the context of optical flow [31, 32, 25, 33, 34, 35, 36] or geometric matching [26, 27, 28, 29, 25, 62], where image pairs are from consecutive frames in a video or from different views of the same scene.

Dense matching methods can be either supervised or unsupervised. Supervised methods require a carefully designed synthetic dataset with ground-truth flow/displacement annotations [33, 63]. Unsupervised methods, on the other hand, do not require ground-truth annotations. Instead, they often use photometric consistency to encourage the estimated flow or displacement to align locations with similar appearances [64, 25, 65]. At the same time, the spatial smoothness of the estimated flow or displacement is typically assumed and enforced. For example, RANSAC-Flow [25] uses the photogrammetric loss combined with the cycle consistency between the forward and backward flow estimation. It combines both sparse and dense matching methods by using sparse features to pre-align images with homography and then estimates the per-pixel dense optical flow using neural networks. Another approach of unsupervised dense matching synthesizes warps of real images by combining different geometric transformations and uses the synthesized flow/displacement for self-supervision [27, 28, 62, 26]. Those methods can handle larger displacements by adjusting the amplitude of the synthesized warp and are robust against appearance changes without relying on photometric losses. GLU-Net [27] integrates both global and local feature correlations to handle large and small displacements. Direct supervision trains the network to regress a randomly sampled displacement field, but this often results in poor generalization to real image pairs. To solve this problem, WarpC-GLU-Net [29] introduces an image triplet strategy, combining real image pairs with a randomly warped version of one image and enforcing consistency within the triplet. Starting from this method, we add map-specific disturbances, i.e. changes and randomly displaced texts, to enhance the displacement estimation for aligning historical maps.

.2 Historical map registration and alignment

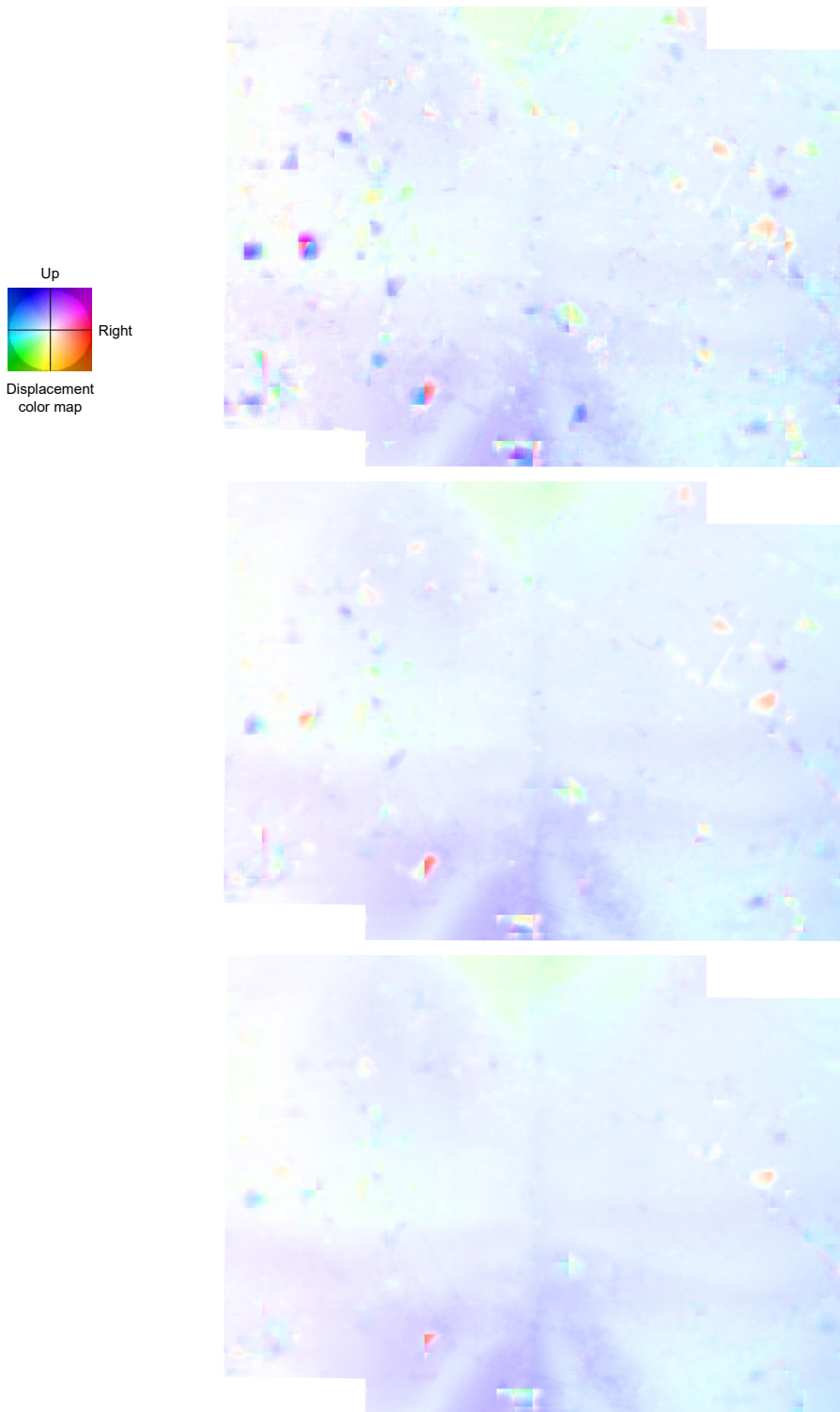
In existing research, map registration is often treated as a step within the geo-referencing process, where coordinates are assigned to maps by comparing them with reference maps or other geospatial data, typically

using control points [66, 67, 68], image features [69, 70], extracted objects [71, 72, 73]. [74] introduced a geographic knowledge graph (GKG), an organized collection of entities and concepts interconnected through their relationships, allowing the identification of the same object at different years. However, their pipeline required control points to perform subsequent geometric transformations. Although these methods are effective, they typically depend on a single pre-defined or explicitly identified geometric transformation. In a novel approach, [18] employed deep neural networks to directly establish dense correspondences between maps, which can handle non-geometric deformation and is fully automated without defining the transformations and control points. Yet, this approach remains sensitive to object changes and text displacements, which can introduce significant distortions in the alignment process.

.3 Historical map segmentation

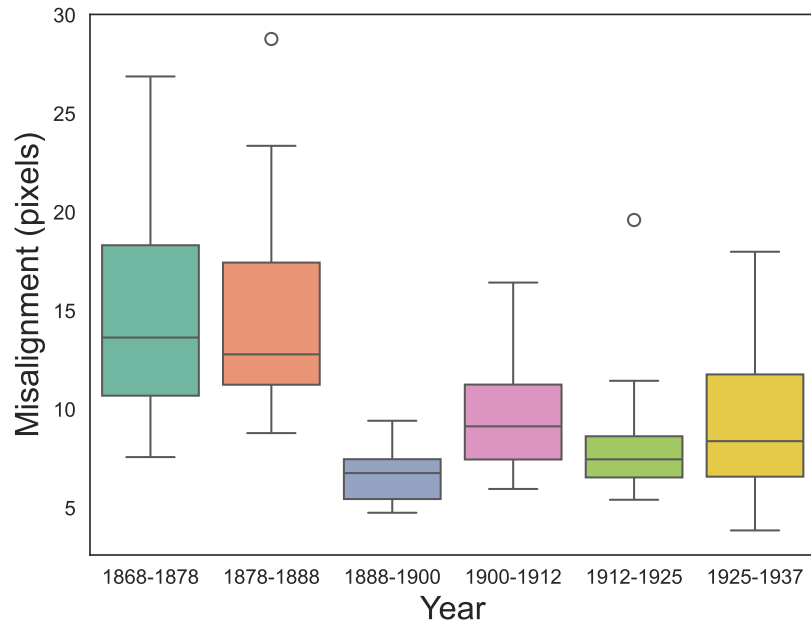
Unlocking the information from historical maps offers valuable insights into past landscapes and the spatio-temporal evolution of Earth’s features. Processing these maps has become an interdisciplinary effort between cartography, geoinformatics, and computer vision. In contrast to methods that rely on manual interventions [75, 76, 77] or map-specific fine-tuning of certain features [78, 79, 80], deep learning has facilitated the automated segmentation of historical maps. This includes detecting roads [81, 12, 82], buildings and blocks [17, 16, 83, 12], water bodies [13, 84, 85], and text [86, 87], using CNNs and transformers. While these works mainly address texture-rich maps, [83, 88, 14] focused on segmenting building instances from texture-less maps, specifically the *Atlas Municipal*, by conducting edge detection first and consequently converting the detected edges to closed polygons that form building instances. However, these edge-based methods fail to detect sidewalks—key elements of urban infrastructure—typically represented with open borders in maps.

Supplementary Note 5: Qualitative comparison of estimated displacement field



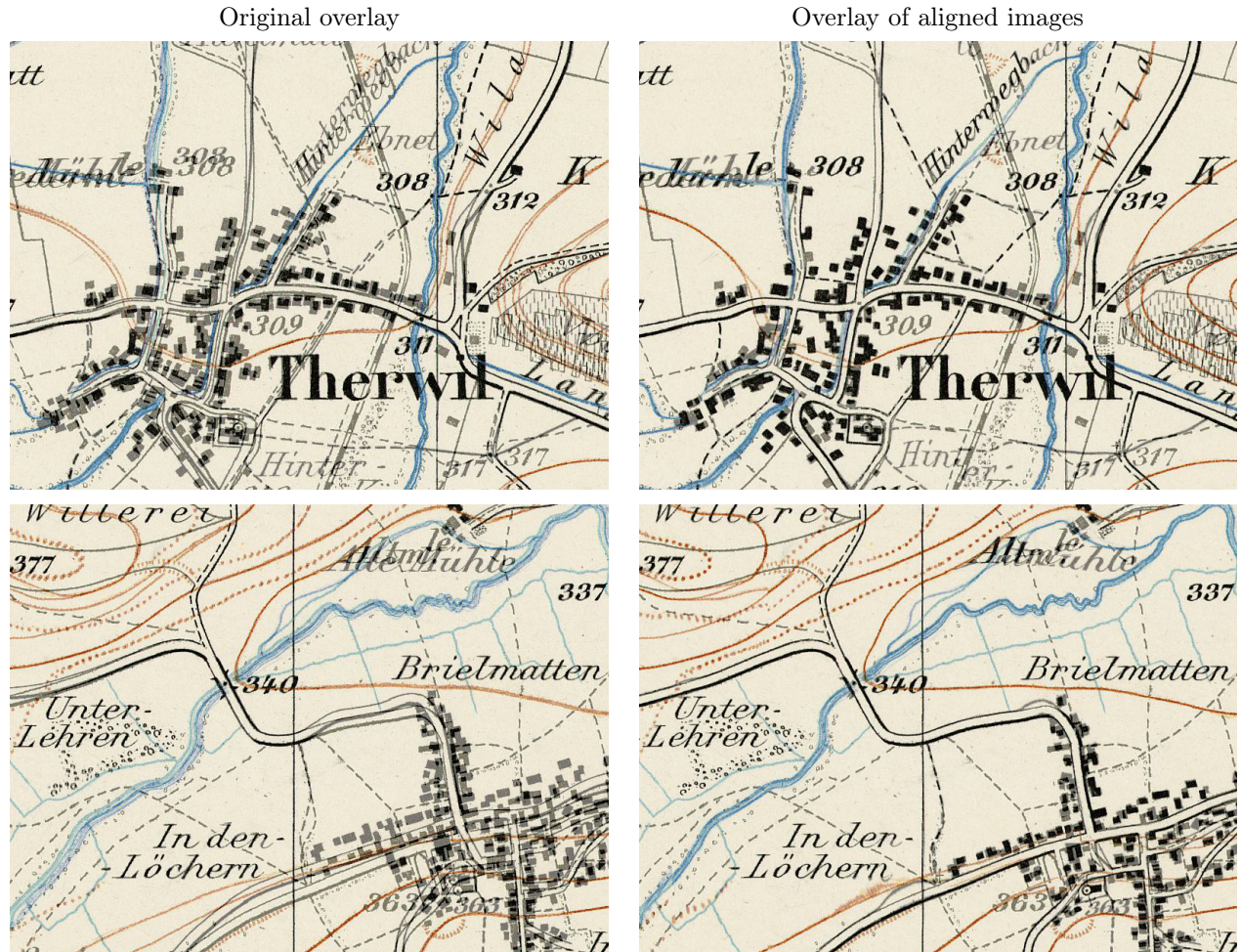
Supplementary Fig. S4: A qualitative comparison of the estimated displacement field tested on maps of the same area from the years 1905 and 1937. The results, shown from top to bottom, include GluNet, WarpC, and our method. Our model outperforms the others by generating a smoother displacement field and effectively revealing the upward-right shift and the paper-folding artifacts.

Supplementary Note 6: Applications of displacement estimation for map distortion studies



Supplementary Fig. S5: Misalignment (in pixels) between maps over time. For each region, we compute the median of estimated per-pixel displacement, and the boxplot summarizes their distribution across all regions. This illustrates the potential of displacement estimation for analyzing map distortions and the evolution of cartographic techniques.

Supplementary Note 7: Additional results on other maps



Supplementary Fig. S6: We re-train our alignment model on Siegfried maps, a topographic map series from Switzerland at the scale of 1:25000. Our model achieves plausible results in aligning various types of landscape features, highlighting its generalizability across different map types and scales.

Supplementary Note 8: Additional figures on label propagation



Supplementary Fig. S7: Example of propagated labels from 1925 to 1905, shown in edge maps. Top: the original edge map from 1925, which exhibits clear misalignment with the map from 1905. Bottom: the edge map propagated using the estimated displacement field from 1925 to 1905. The propagated labels align closely with the target map, illustrating the ability of the proposed method to transfer annotations accurately across decades despite substantial urban change and cartographic variation.